



α -Fe₂O₃/SnO₂ heterostructure composites: A high stability anode for lithium-ion battery



Yanhua Ding, Bing Liu, Jiajia Zou, Huanqing Liu, Tuo Xin, Linhua Xia*, Yiqian Wang*

College of Physics, Qingdao University, No. 308 Ningxia Road, Qingdao, 266071, PR China

ARTICLE INFO

Keywords:
Composites
Oxides
Chemical synthesis
Microstructure
Electrochemical properties

ABSTRACT

α -Fe₂O₃ microoval structure decorated with SnO₂ nanocrystals are fabricated by hydro-thermal process. The composite heterostructure has a uniform size of 310 nm in length and 110 nm in width, and SnO₂ shell thickness is ~10 nm. The SnO₂ shell acts as a conductive layer to offer fast pathways for transport of electrons and ions. What is more, the SnO₂ layer serves as an inactive matrix for α -Fe₂O₃ particles, avoiding agglomeration and keeping structural integrity. Benefiting from the smart design, the hierarchical α -Fe₂O₃/SnO₂ composite as anode exhibits a higher specific capacity and a better rate performance than those of pristine α -Fe₂O₃ structures. The stability electrochemical performance of the hierarchical composite can be put down to the core-shell architecture, which improves the conductivity and stability of the electrodes. The heterostructure design in our work provides a possible approach to synthesis high stability materials for electrochemical energy storage.

1. Introduction

Rechargeable batteries with high power/energy density, long cycle life and high safety have been developed for a variety of applications, such as portable consumer electronic products, electromobiles and large-scale energy storage in smart grids [1]. However, the commercial batteries cannot meet the fast-growing demand, thereby attracting much interest and prompting extensive studies [2–4]. For lithium-ion batteries (LIBs), graphite or modified graphite has become the most popular negative electrode materials, but its theoretical specific capacity is only 372 mA h g⁻¹. The main challenge in this field is that the graphite-based materials used in commercial LIBs cannot satisfy the demand of higher energy density. Thus, great efforts have been devoted to exploring negative electrode materials with a high specific capacity [5–7]. Recently, transition metal oxides (Fe₂O₃, SnO₂, Co₃O₄, Fe₃O₄, etc.) have been widely investigated due to their high theoretical capacity, natural abundance and environmentally friendly [8].

Among various metal oxides, α -Fe₂O₃ has a higher theoretical specific capacity, nearly three times that of graphite [9–11]. Drastic volume expansion/shrink will take place during the lithium-ion insertion/extraction process for α -Fe₂O₃-based materials, leading to pulverization and aggregation of α -Fe₂O₃ and large irreversible capacity loss. SnO₂ as negative electrode has been reported due to its high reversible capacity and high conductivity, but with tremendous volume expansion and lower coulombic efficiency (CE) [12–14]. One of the approaches to circumvent these obstacles is to synthesize nanostructured oxide/

graphene, such as Fe₂O₃/graphene and SnO₂/graphene [15,16]. Recent advances have moved to engineer new structures as anode materials of LIBs with a special design to improve their physical and chemical properties, i.e. heterostructured composites [17–19]. Zhou et al. [20] reported a branched heterostructure composed of SnO₂ and α -Fe₂O₃, which shows a remarkably-improved capacity of 800 mA h g⁻¹, much higher than that of pure SnO₂ (230 mA h g⁻¹) and α -Fe₂O₃ (300 mA h g⁻¹). Lou et al. [21] reported SnO₂ submicroboxes with a SnO₂ shell thickness of 40 nm, which delivered a reversible specific capacity of 491 mA h g⁻¹ at 0.5 A g⁻¹ after 100 cycles. Some studies have suggested that the strain due to the volume change during Li-ion insertion/extraction cycling could be avoided by introduce nanosized materials [22–24] or integrate carbon materials as structural buffers [25,26], thereby enhancing the cycle stability. These strategies can relieve strain and promote electron transport to partly improve the performance of LIBs, but the cycling performance is still unsatisfactory in the previous reports on SnO₂ and α -Fe₂O₃ [22,27]. Thus, it is highly expected that α -Fe₂O₃/SnO₂ composites should have excellent performances due to the interaction of the two components. To our best knowledge, there is no report on preparation of heterostructured composites of α -Fe₂O₃ microovals decorated with SnO₂ nanocrystals (NCs) as negative electrode materials for LIBs.

In this work, α -Fe₂O₃/SnO₂ heterostructure composites decorated with SnO₂ NCs are synthesized via a two-step hydrothermal method. Benefiting from the structural features and synergistic effect, the α -Fe₂O₃/SnO₂ anode exhibits high stability lithium storage performance

* Corresponding authors.

E-mail addresses: lhx@qdu.edu.cn (L. Xia), yqwang@qdu.edu.cn (Y. Wang).

for LIBs. The lithium storage mechanism of the $\alpha\text{-Fe}_2\text{O}_3/\text{SnO}_2$ electrode was also investigated by examining its microstructural evolution after discharge/charge cycling.

2. Experimental section

2.1. Materials preparation

The synthesis of $\alpha\text{-Fe}_2\text{O}_3/\text{SnO}_2$ composites follows two steps. Firstly, the $\alpha\text{-Fe}_2\text{O}_3$ microovals were prepared by following our previous work [28]. Secondly, 100 mg $\alpha\text{-Fe}_2\text{O}_3$ microovals was dispersed in 30 mL deionized (DI) water by ultrasonication to form a suspension. Then 1 mmol Na_2SnO_3 was dissolved in another 30 mL DI water and added to the former suspension under constant stirring. The obtained suspension was transferred to Teflon-lined stainless steel autoclave, which was heated at 180 °C for 24 h. The resultant product was collected by centrifuged with DI water and ethanol, dried in an oven at 60 °C overnight.

2.2. Materials characterization

Powder x-ray diffraction (XRD) patterns were obtained with a Rigaku SmartLab X-ray diffractometer using $\text{Cu-K}\alpha$ radiation ($\lambda = 1.5406 \text{ \AA}$). Field-emission scanning electron microscopy (FESEM) and energy-dispersive x-ray spectroscopy (EDS) were carried out on a Hitachi S-4800 scanning electron microscopy (SEM). Bright-field (BF) transmission electron microscopy (TEM) imaging, selected-area electron diffraction (SAED), high-resolution transmission electron microscopy (HRTEM) imaging, and TEM-EDS element mapping of the samples were performed on a JEOL JEM2100 F electron microscope with an acceleration voltage of 200 kV. X-ray photoelectron spectra (XPS) were recorded on an ESCALAB 250 spectrometer with a monochromatic Al $\text{K}\alpha$ radiation ($h\nu = 1486.6 \text{ eV}$) under ultrahigh vacuum (below 10^{-8} Pa).

2.3. Electrochemical measurements

Electrochemical measurements were conducted by half coin-type cells (CR2025) assembled inside a glove box (Mikrouna) under an argon atmosphere at room temperature (25 °C). The working electrodes were fabricated by mixing 70 wt.% $\alpha\text{-Fe}_2\text{O}_3/\text{SnO}_2$ or $\alpha\text{-Fe}_2\text{O}_3$, 15 wt.% acetylene black and 15 wt.% sodium-alginate (SA) and adequate amount of DI water, coating the mixture on the copper current collector and drying in a vacuum oven at 120 °C for 12 h. The loading of active material was ca. $0.8 \text{ mg}\cdot\text{cm}^{-2}$. Pure lithium foil was used as a counter electrode, 1 M LiPF_6 in ethylenecarbonate (EC) and dimethyl carbonate (DMC) (EC:DMC = 1:1 in volume) as electrolyte and a polypropylene microporous film as separator. The galvanostatic charge-discharge tests were performed on LAND CT 2001A battery testing system in a voltage range from 0.01 to 3.0 V vs. Li/Li^+ . Cyclic voltammetry (CV) was performed on Metrohm Autolab PGSTAT302N in a potential window of 0.01–3.0 V with a scan rate of $0.1 \text{ mV}\cdot\text{s}^{-1}$. Electrochemical impedance spectroscopy (EIS) was performed on fresh cells at open circuit potential with Metrohm Autolab PGSTAT302N by applying a sine wave with an amplitude of 5.0 mV over a frequency range from 100 kHz to 0.1 Hz.

3. Results and discussion

The crystal structures of as-prepared products were analyzed by XRD, as displayed in Fig. 1(a). In these patterns, the main diffraction peaks of the products match well with those of rhombohedral $\alpha\text{-Fe}_2\text{O}_3$ (JCPDF: 33-0664) [29]. The weak diffraction peaks marked by inverted triangles can be ascribed to tetragonal rutile SnO_2 (JCPDF: 41-1445), and the relatively low diffraction intensity is due to the low content and small crystal size of SnO_2 in the samples. It is shown that the incorporation of SnO_2 has no impact upon $\alpha\text{-Fe}_2\text{O}_3$ crystalline structure,

because the diffraction peaks of the hematite phase in the samples locate in the standard $\alpha\text{-Fe}_2\text{O}_3$ peak positions. Moreover, the EDS spectrum further demonstrates the existence of SnO_2 in the samples, as shown in Fig. 1(b). It reveals that the product consists of four elements (C, O, Fe, Sn), and the weight percentages of Fe and Sn elements are about 42% and 14%, respectively. The quantification of EDS spectrum shows that the molar ratio of $\alpha\text{-Fe}_2\text{O}_3$ and SnO_2 is about 6:1. The C element may originate from the residual surfactants of PVP.

Fig. 2 shows typical XPS spectra of $\alpha\text{-Fe}_2\text{O}_3/\text{SnO}_2$ composites, indicating the existence of Fe, C, Sn, and O elements. In Fig. 2(a), the spectra exhibit two broad peaks at around 724.3 eV and 710.6 eV, corresponding to Fe $2p_{1/2}$ and Fe $2p_{3/2}$ states, respectively [30]. The satellite peak at around 718.9 eV gives further evidence of $\alpha\text{-Fe}_2\text{O}_3$. For C 1s spectra in Fig. 2(b), three peaks are assigned to C = O (287.8 eV), C = N (286.5 eV), C-C (284.7 eV), indicating the presence of residual surfactant of PVP [31]. The peaks located at 716.5 eV, 494.6 eV and 486.1 eV in Fig. 2(a) and (c) are attributed to Sn $3p_{3/2}$, Sn $3d_{3/2}$ and Sn $3d_{5/2}$, respectively, confirming the presence of SnO_2 in the composites [32,33]. Fig. 2(d) displays the XPS spectra of O 1s, in which the binding energy peaks at 531.5 and 529.6 eV represent Fe-O and Sn-O, respectively, corresponding to O^{2-} from $\alpha\text{-Fe}_2\text{O}_3$ and SnO_2 [34]. These results further confirm that the composites consist of $\alpha\text{-Fe}_2\text{O}_3$, SnO_2 and carbon.

Morphology and microstructure about $\alpha\text{-Fe}_2\text{O}_3/\text{SnO}_2$ composites were further examined by FESEM and TEM. Fig. 3(a) and (b) show typical FESEM images of the $\alpha\text{-Fe}_2\text{O}_3/\text{SnO}_2$ composites at different magnifications. It is clearly revealed that the composites are oval-like with a relatively uniform size. The dimensions of the composites are about 310 nm in length and about 110 nm in width, and the surface of the composites is covered with many NCs. Fig. 3(c) reveals BF TEM image of single $\alpha\text{-Fe}_2\text{O}_3/\text{SnO}_2$ structure, where a core-shell structure is observed. To clarify the microstructure of $\alpha\text{-Fe}_2\text{O}_3/\text{SnO}_2$ composite, HRTEM image was performed, as displayed in Fig. 3(d). The crystal lattice spacings measured from the HRTEM image are 2.70 Å and 3.35 Å, which correspond to the (10 $\bar{1}$ 4) planes of $\alpha\text{-Fe}_2\text{O}_3$ and (110) planes of SnO_2 , respectively. In the core-shell structure, the core is $\alpha\text{-Fe}_2\text{O}_3$ microoval, while the shell is composed of SnO_2 NCs. The average shell of SnO_2 layer is $\sim 10 \text{ nm}$. To better investigate the distribution of Fe, Sn, O and C in the composite, elemental mappings were obtained for the individual core-shell structure as demonstrated in Fig. 3(e)–(h). The Fe element is mainly distributed in the core, while the Sn element is mainly located in the outer layer of the core-shell structure. In addition, the O and C elements are evenly distributed in an individual composite, and the C around the microoval is attributed to the carbon film on the copper grids to support sample. Therefore, the $\alpha\text{-Fe}_2\text{O}_3$ microovals were uniformly decorated with SnO_2 NCs on the whole surface.

According to the above analysis, the synthetic process of $\alpha\text{-Fe}_2\text{O}_3/\text{SnO}_2$ composites is schematically illustrated in Fig. 4. Firstly, PVP acts as surfactant to prevent the nanoparticles from agglomeration in the DI water and ethanol solution of FeCl_3 and PVP. The reaction between Fe^{3+} ions and ethylenediamine (EDA) probably forms Fe^{3+} -EDA complex after the addition of the EDA. The stability of the complex decreases at high temperature and unstable coordinated ligands disappear. The Fe^{3+} freedom and react to OH^- from water to form $\text{Fe}(\text{OH})_3$ in this process. When the solution mixture is transferred to the autoclave and heated at 180 °C, $\text{Fe}(\text{OH})_3$ particles grow and evaporated to form oval-like $\alpha\text{-Fe}_2\text{O}_3$ particles [35,36]. Secondly, the SnO_3^{2-} ions are gradually released from the added Na_2SnO_3 , and will aggregate on the surface of $\alpha\text{-Fe}_2\text{O}_3$. The SnO_2 NCs are grown on the surface of $\alpha\text{-Fe}_2\text{O}_3$ under the mild hydrothermal conditions. Finally, the heterostructured composites of $\alpha\text{-Fe}_2\text{O}_3/\text{SnO}_2$ are produced.

The electrochemical properties of $\alpha\text{-Fe}_2\text{O}_3/\text{SnO}_2$ heterostructures is first evaluated by CV, which helps to better understand the redox reactions. Fig. 5(a) displays a typical CV of $\alpha\text{-Fe}_2\text{O}_3/\text{SnO}_2$ heterostructures in the potential window of 0.01–3.00 V at a scan rate of 0.1 mV/s. In first cathodic process, four reduction peaks can be

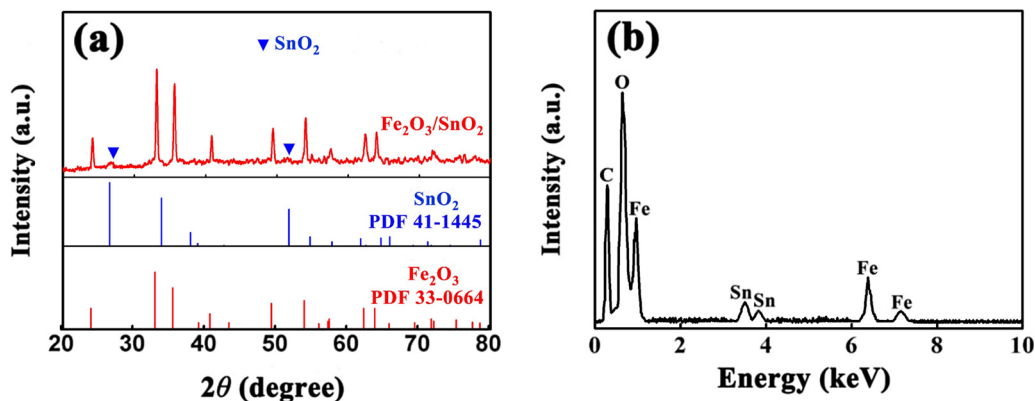


Fig. 1. (a) XRD patterns of the products; (b) Typical EDS spectrum of α - $\text{Fe}_2\text{O}_3/\text{SnO}_2$ composites.

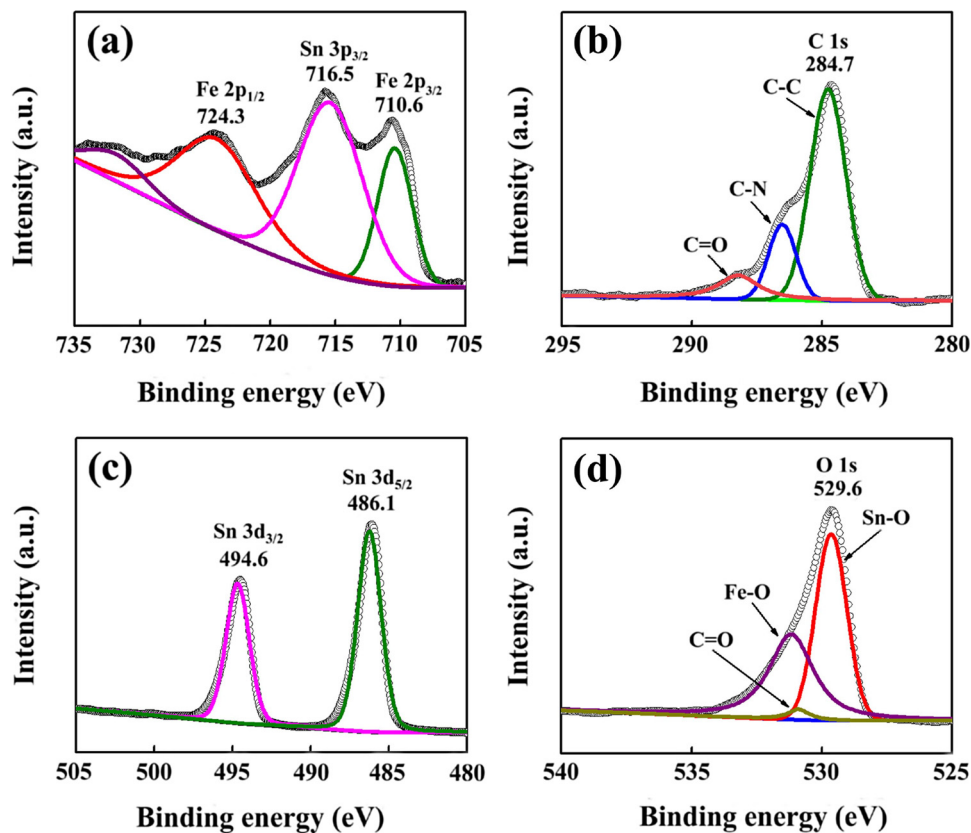


Fig. 2. XPS spectra of α - $\text{Fe}_2\text{O}_3/\text{SnO}_2$ composites. (a) Fe 2p and Sn 3p; (b) C 1s; (c) Sn 3d; (d) O 1s.

observed at 1.2, 0.9, 0.6 and 0.1 V, respectively. A pair of cathodic peaks located at 1.2 and 0.6 V are associated with the reduction of Fe^{3+} into metallic Fe^0 ($\text{Fe}_2\text{O}_3 + 2\text{Li}^+ + 2\text{e}^- \rightarrow \text{Li}_2(\text{Fe}_2\text{O}_3)$, $\text{Li}_2(\text{Fe}_2\text{O}_3) + 4\text{Li}^+ + 4\text{e}^- \rightarrow 2\text{Fe} + 3\text{Li}_2\text{O}$) [37,38], while the peaks observed at 0.9 and 0.1 V are assigned to the reduction of SnO_2 to Sn ($\text{SnO}_2 + 4\text{Li}^+ + 4\text{e}^- \rightarrow \text{Sn} + 2\text{Li}_2\text{O}$), and lithium insertion into Sn to form a Li_xSn alloy ($\text{Sn} + x\text{Li} + \text{xe}^- \rightarrow \text{Li}_x\text{Sn}$) [39]. The strong non-reversible cathodic peak at around 0.6 V is ascribed to the forming of solid electrolyte interphase (SEI), which disappears after first cycle. Furthermore, two oxidation peaks are located at 0.55 and 1.8 V. The weak anodic peak at 0.55 V is due to dealloying reaction of Li_xSn alloy ($\text{Li}_x\text{Sn} \rightarrow \text{Sn} + x\text{Li}^+ + \text{xe}^-$). The broad anodic peak at around 1.8 V is assigned to the metallic Fe into Fe^{3+} ($2\text{Fe} + 3\text{Li}_2\text{O} \rightarrow \text{Fe}_2\text{O}_3 + 6\text{Li}^+ + 6\text{e}^-$) and partial reversible formation of SnO_2 ($\text{Sn} + \text{Li}_2\text{O} \rightarrow \text{SnO}_2 + 4\text{Li}^+ + 4\text{e}^-$) [40]. In subsequent cycles, a couple of peaks located at 0.02 and 0.55 V (cathodic/anodic) can be attributed to reversible alloying and

dealloying reactions of Li_xSn ($0 \leq x \leq 4.4$). Another couple of peaks observed at 0.88 and 1.8 V (cathodic/anodic) are caused by reversible oxidation-reduction reactions of α - Fe_2O_3 [20]. The CV of pure α - Fe_2O_3 is shown in Fig. S1 [28]. The peak observed at 0.5 V is attributed to the formation of SEI film and the reduction of α - Fe_2O_3 to Fe. The anodic peak at 1.8 V during the first cycle can be ascribed to the oxidation of Fe (0) to Fe^{3+} . Compared to the CV of the pure α - Fe_2O_3 , α - $\text{Fe}_2\text{O}_3/\text{SnO}_2$ composite electrode has extra peaks, corresponding to the redox reactions of SnO_2 . The lithiation-delithiation potentials of SnO_2 are lower than those of α - Fe_2O_3 . Thus, the SnO_2 layer in the composite serves as inactive matrices to prevent α - Fe_2O_3 microovals from agglomeration during discharge-charge cycling.

Fig. 5(b) displays the 1st, 2nd, 100th and 150th discharge/charge profiles of α - $\text{Fe}_2\text{O}_3/\text{SnO}_2$ electrode at $100 \text{ mA} \cdot \text{g}^{-1}$. The first discharge curve exhibits a wide voltage plateau at $\sim 0.88 \text{ V}$, in good agreement with above CV results. The initial discharge/charge specific capacities

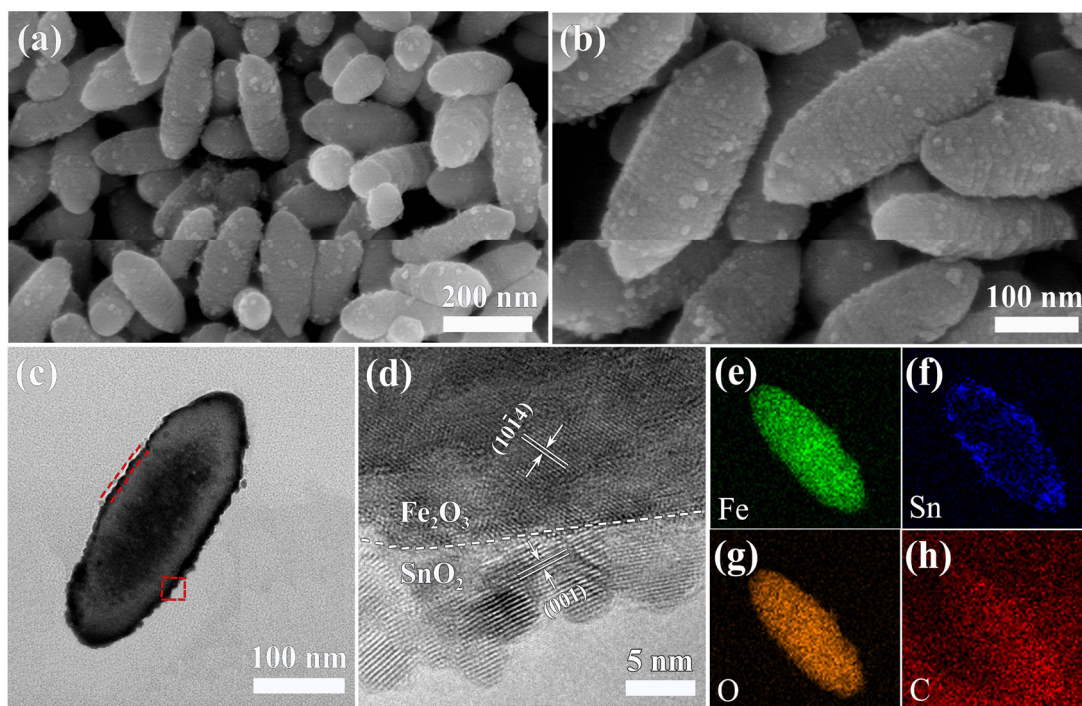


Fig. 3. (a) and (b) FESEM images of α -Fe₂O₃/SnO₂ composites; (c) BF TEM image of single α -Fe₂O₃/SnO₂ structure; (d) HRTEM image of square region in (c); (e–h) TEM-EDS elemental mapping of Fe, O, Sn, C in an individual composite.

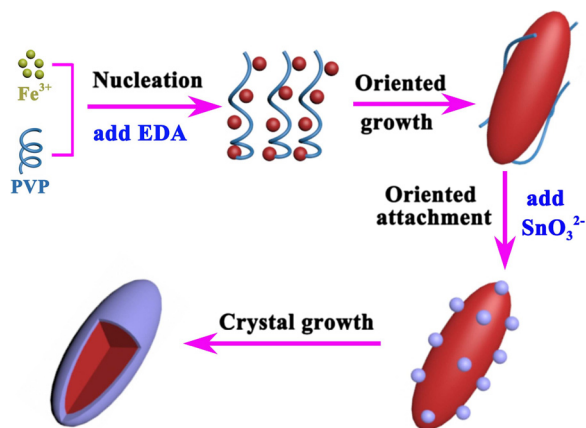


Fig. 4. Schematic illustration of the formation of α -Fe₂O₃/SnO₂ composites.

of α -Fe₂O₃/SnO₂ are 1262 and 902 mA h g⁻¹, corresponding to a CE of 71%. The irreversible capacity reduction can be assigned to the decomposition in the electrolyte or some non-reversible reactions such as the formation of SEI layer in the initial discharge cycle [41]. During the second cycle, the discharge and charge specific capacities are 909.2 mA h g⁻¹ and 892.6 mA h g⁻¹, respectively. The capacity is maintained at a stable level in the following cycles, and the 100th and 160th galvanostatic discharge and charge curves are highly coincident, indicating that the as-prepared α -Fe₂O₃/SnO₂ composites have prominent cycling stability. The charge/discharge profile of pure α -Fe₂O₃ is shown in Fig. S2 [28]. A distinct long voltage platform can be clearly seen at \sim 0.8 V in the first discharge curve, and a sloping platform at \sim 2.0 V is observed due to a reverse reaction in the first charge curve in good agreement of the CV results. The reversible capacity of pure α -Fe₂O₃ electrode is higher than that of α -Fe₂O₃/SnO₂ electrode during 1–50 cycles. The results further demonstrated that the introduced SnO₂ can react with Li⁺ in the low lithiation-delithiation potentials.

Fig. 5(c) depicts cycling performance of α -Fe₂O₃/SnO₂ and α -Fe₂O₃ structured electrodes, and CE of α -Fe₂O₃/SnO₂ composites from the

first cycle to the 160th cycle at 100 mA g⁻¹ between 0.01 and 3.0 V. The α -Fe₂O₃/SnO₂ structured electrode exhibits a discharge capacity of 817 mA h g⁻¹ after 160 cycles, which is nearly three times of the pure α -Fe₂O₃ (304 mA h g⁻¹ after 160 cycles). The composite electrode shows superior capacity retention in electrochemical cycling process. Compared with pure α -Fe₂O₃ electrode, the α -Fe₂O₃/SnO₂ electrode shows remarkable cycling performance because the introduced SnO₂ is able to prevent the electrode in the process of lithiation-delithiation [42].

Besides the cycling behavior, rate capability is also an important factor for LIBs. As shown in Fig. 5(d), α -Fe₂O₃/SnO₂ composites deliver discharge capacities of around 783, 702, 601, 498, 389, 780 mA h g⁻¹ at 0.1, 0.2, 0.5, 1, 2 and 0.1 A g⁻¹, respectively. The discharge capacity of 780 mA h g⁻¹ is obtained when current density returns to 0.1 A g⁻¹ after 50 cycles. More remarkably, the electrode of α -Fe₂O₃/SnO₂ composite is more stable than the α -Fe₂O₃ microovals electrode in long cycling life. The enhanced rate performance of the α -Fe₂O₃/SnO₂ electrode can be allied to the promoted conductivity of the heterostructures after being decorated with the SnO₂ layer. Therefore, the incorporation of SnO₂ NCs onto the surface of α -Fe₂O₃ microovals can improve the cycle performance of LIBs.

To further demonstrate the excellent electrochemical performance, EIS measurements were conducted on α -Fe₂O₃/SnO₂ composites and α -Fe₂O₃ microovals. As shown in Fig. 6(a), the Nyquist plots are composed of a semicircle at high frequency and an inclined line at low frequency [43,44]. The impedance data are fitted by the equivalent circuit shown as the inset in Fig. 6(a), in which R_s and R_{ct} represent ohmic resistance and charge transfer resistance, CPE is double-layer capacitance, and W is the Warburg impedance. The semicircle of the α -Fe₂O₃/SnO₂ composites is relatively small as compare to α -Fe₂O₃ microovals. The fitted value of R_{ct} for α -Fe₂O₃/SnO₂ electrode (R_{ct} = 19.5 Ω) is lower than that for α -Fe₂O₃ electrode (R_{ct} = 31.6 Ω), indicating that the SnO₂ layer can accelerate ion diffusion and decreases the total internal resistance of the battery, leading to a significant enhancement in the electrochemical performance [45]. The lithium ion diffusion coefficient (D_{Li}) is calculated according to the formula $D_{Li} = R^2 T^2 / 2A^2 n^4 F^4 C^2 \sigma^2$, where R is the ideal gas constant, T is the absolute

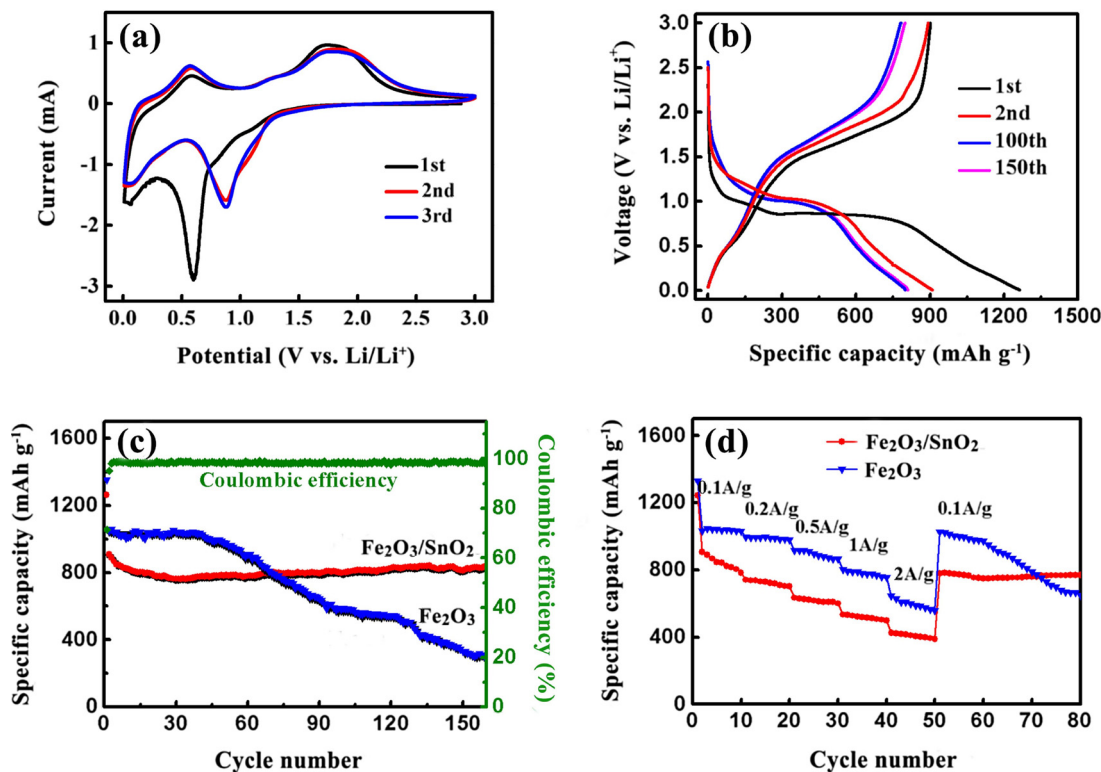


Fig. 5. (a) Typical CV of the α -Fe₂O₃/SnO₂ composites; (b) Discharge/charge curves of α -Fe₂O₃/SnO₂ composites; (c) Cycling performance of α -Fe₂O₃/SnO₂ composites and α -Fe₂O₃ microovals at 0.1 A g⁻¹, and CE of α -Fe₂O₃/SnO₂ composites; (d) Rate performance of α -Fe₂O₃/SnO₂ composites and α -Fe₂O₃ microovals.

temperature, A is the cross-sectional area of the electrode, n is the number of transferred electron per molecule, F is Faraday constant, C is the electrode of lithium ion concentration, and σ is Warburg factor. As shown in Fig. 6(b), the relationship between σ and Z' can be described using $Z' = R_s + R_{ct} + \sigma\omega^{-1/2}$, where Z' is the real part of the impedance spectrum, R_s is the solution resistance, R_{ct} is the charge transfer, ω is the angular frequency, and σ is the value of the slope of the curve. From Fig. 6(b), the σ values of α -Fe₂O₃/SnO₂ and α -Fe₂O₃ electrodes are determined to be 90.65 and 159.28, respectively. The corresponding lithium ion diffusion coefficients of α -Fe₂O₃/SnO₂ and α -Fe₂O₃ electrode are calculated to be 1.81×10^{-6} cm²s⁻¹ and 5.87×10^{-7} cm²s⁻¹, respectively. The lithium ion diffusion coefficient of the α -Fe₂O₃/SnO₂ is higher than that of α -Fe₂O₃, indicating fast Li-ion diffusion in the α -Fe₂O₃/SnO₂ electrode. Therefore, the introduction of the SnO₂ layer can improve the conductivity of the active material and enhance the electrochemical reaction.

To further understanding the electrochemical property of the α -Fe₂O₃/SnO₂ electrode, TEM, HRTEM and SAED were employed to investigate its microstructural change in the delithiated states (3.0 V) after 160 cycles at 0.1 A g⁻¹. Fig. 7(a) and (b) show typical BF TEM images of the α -Fe₂O₃/SnO₂ electrode after 160 cycles. The morphology of active materials remains oval-like shape, while their length and width are much bigger than those dimensions before cycling. No obvious cracks and breakage can be found, suggesting that the composites well accommodate the volume changes during cycling. Fig. 7(c) shows an enlarged TEM image of interface area surrounded by a small rectangle in (a), and the corresponding SAED pattern is demonstrated in Fig. 7(e). The diffraction rings in Fig. 7(e) can be indexed using α -Fe₂O₃ and SnO₂. Fig. 7(d) is an enlarged HRTEM image surrounded by a rectangle in (c). To obtain more detailed microstructural information, enlarged HRTEM images of different areas are shown in Fig. 7(f–h). The HRTEM images show crystal lattices with an interplanar distance of

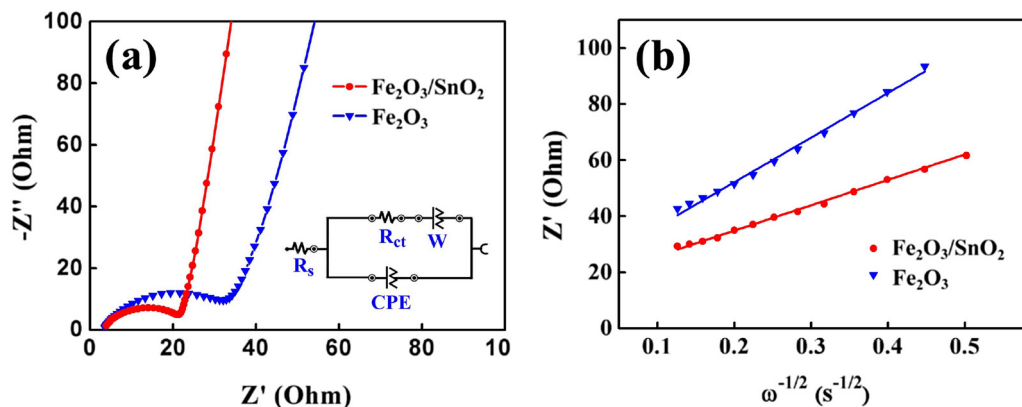


Fig. 6. (a) The impedance spectra of α -Fe₂O₃/SnO₂ composites and α -Fe₂O₃ microovals, inset is an equivalent circuit; (b) The relationship between Z' and $\omega^{-1/2}$ in the low frequency region.

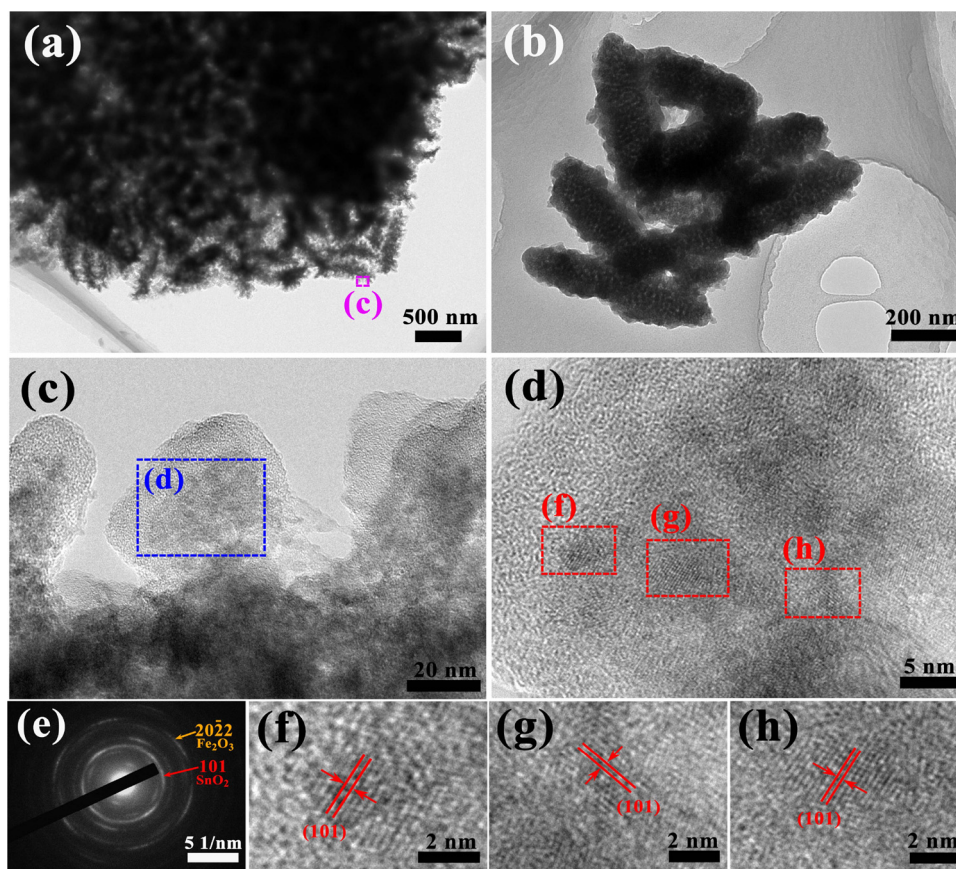


Fig. 7. TEM images and SAED pattern of the α - $\text{Fe}_2\text{O}_3/\text{SnO}_2$ electrode after 160 cycles. (a) and (b) BF TEM images; (c) Enlarged TEM image of interface area enclosed by the rectangle in (a); (d) Enlarged HRTEM image of the region in (c); (e) Typical SAED pattern taken from (c); (f), (g), (h) HRTEM images of different areas in (d).

2.60 Å that can be ascribed to (101) planes of SnO_2 . This reveals that the SnO_2 NCs are still coated on the surface of α - Fe_2O_3 during the delithiation process, thus the SnO_2 can well protect the α - Fe_2O_3 during the discharge/charge cycling.

The remarkable cycling stability and rate performance of hierarchical α - $\text{Fe}_2\text{O}_3/\text{SnO}_2$ composites can be attributed to the complementary roles of SnO_2 and α - Fe_2O_3 . First, the SnO_2 layer can provide a fast transport pathway for both electrons and ions, as well as act as a structural buffer to accommodate the volume expansion/shrinkage during the cycling. Second, the potentials of SnO_2 for both lithium insertion and extraction are lower than those of α - Fe_2O_3 , thus the thin SnO_2 layer can play the part of inactive matrix for α - Fe_2O_3 particles, avoiding agglomeration and keeping structural integrity. On the basis of above advantages, the lithium storage performance of α - $\text{Fe}_2\text{O}_3/\text{SnO}_2$ composite anode are significantly improved, compared with pure α - Fe_2O_3 .

4. Conclusions

In summary, hierarchical α - $\text{Fe}_2\text{O}_3/\text{SnO}_2$ composites with an average SnO_2 shell thickness of ~ 10 nm were synthesized through a two-step hydrothermal method. The SnO_2 NCs were uniformly decorated onto the outside surface of α - Fe_2O_3 microovals. When evaluated as anode material for LIBs, the composite delivers a specific capacity of over 810 mA h g^{-1} at 100 mA g^{-1} after 160 cycles, better than that of pristine α - Fe_2O_3 . The stability electrochemical performance of the hierarchical composite can be put down to the core-shell architecture, which reduces its internal resistance of the battery, and improves the conductivity of the electrodes and stabilizes α - Fe_2O_3 structures. Further design and regulate of a core-shell heterostructured material will open a new opportunity in the areas of photoconversion, sensing and

electrochemical energy storage.

Acknowledgements

The research was supported by National Natural Science Foundation of China (Grant No.: 21701095), Natural Science Foundation for Outstanding Young Scientist in Shandong Province (Grant no.: JQ201002), High-end Foreign Experts Recruitment Programs (Grant No.: GDW20173500154), Top-notch Innovative Talent Program of Qingdao City (Grant No.: 13-CX-08). Y. Q. Wang would also like to thank the financial support from the Taishan Scholar Program of Shandong Province, and Qingdao International Center for Semiconductor Photoelectric Nanomaterials and Shandong Provincial University Key Laboratory of Optoelectrical Material Physics and Devices.

Appendix A. Supplementary data

Supplementary data associated with this article can be found, in the online version, at <https://doi.org/10.1016/j.materresbull.2018.05.014>.

References

- [1] A. Magasinski, P. Dixon, B. Hertzberg, A. Kvit, J. Ayala, G. Yushin, High-performance lithium-ion anodes using a hierarchical bottom-up approach, *Nat. Mater.* 9 (2010) 353–358.
- [2] N. Nitta, F. Wu, J.T. Lee, G. Yushin, Li-ion battery materials: present and future, *Mater. Today* 18 (2015) 252–264.
- [3] M.-S. Balogun, W. Qiu, F. Lyu, Y. Luo, H. Meng, J. Li, W. Mai, Y. Tong, All-flexible lithium ion battery based on thermally-etched porous carbon cloth anode and cathode, *Nano Energy* 26 (2016) 446–455.
- [4] J.B. Goodenough, K.-S. Park, The Li-ion rechargeable battery: a perspective, *J. Am. Chem. Soc.* 135 (2013) 1167–1176.

- [5] L. Zhang, H.B. Wu, B. Liu, X.W. Lou, Formation of porous SnO₂ microboxes via selective leaching for highly reversible lithium storage, *Energy Environ. Sci.* 7 (2014) 1013–1017.
- [6] J. Zhu, Z. Yin, D. Yang, T. Sun, H. Yu, H.E. Hoster, H.H. Hng, H. Zhang, Q. Yan, Hierarchical hollow spheres composed of ultrathin Fe₂O₃ nanosheets for lithium storage and photocatalytic water oxidation, *Energy Environ. Sci.* 6 (2013) 987–993.
- [7] M.A. Rahman, G. Song, A.I. Bhatt, Y.C. Wong, C. Wen, Nanostructured silicon anodes for high-performance lithium-ion batteries, *Adv. Funct. Mater.* 26 (2016) 647–678.
- [8] M.V. Reddy, G.V. Subba Rao, B.V. Chowdari, Metal oxides and oxysalts as anode materials for Li-ion batteries, *Chem. Rev.* 113 (2013) 5364–5457.
- [9] D. Mhamane, H.-K. Kim, V. Aravindan, K.C. Roh, M. Srinivasan, K.-B. Kim, Rusted iron wire waste into high performance anode (α -Fe₂O₃) for Li-ion batteries: an efficient waste management approach, *Green Chem.* 18 (2016) 1395–1404.
- [10] T.C. Jiang, F.X. Bu, X.X. Feng, I. Shakir, G.L. Hao, Y.X. Xu, Porous Fe₂O₃ nano-frameworks encapsulated within three-dimensional graphene as high-performance flexible anode for lithium-ion battery, *ACS Nano* 11 (2017) 5140–5147.
- [11] W.X. Guo, W.W. Sun, L.-P. Lv, S.F. Kong, Y. Wang, Microwave-assisted morphology evolution of Fe-cased metal-organic frameworks and their derived Fe₂O₃ nanostructures for Li-ion storage, *ACS Nano* 11 (2017) 4198–4205.
- [12] B. Liu, M.H. Cao, X.Y. Zhao, Y. Tian, C.W. Hu, Facile synthesis of ultrafine carbon-coated SnO₂ nanoparticles for high-performance reversible lithium storage, *J. Power Sources* 243 (2013) 54–59.
- [13] L. Xia, S.Q. Wang, G.X. Liu, L.X. Ding, D.D. Li, H.H. Wang, S.Z. Qiao, Flexible SnO₂/N-doped carbon nanofiber films as integrated electrodes for lithium-ion batteries with superior rate capacity and long cycle life, *Small* 12 (2016) 853–859.
- [14] T.Y. Ma, X.N. Yu, H.Y. Li, W.G. Zhang, X.L. Cheng, W.T. Zhu, X.P. Qiu, High volumetric capacity of hollow structured SnO₂@Si nanospheres for lithium-ion batteries, *Nano Lett.* 17 (2017) 3959–3964.
- [15] J. Ye, J. Zhang, F.X. Wang, Q.M. Su, G.H. Du, One-pot synthesis of Fe₂O₃/graphene and its lithium-storage performance, *Electrochim. Acta* 113 (2013) 212–217.
- [16] J. Zhang, L. Chang, F.X. Wang, D. Xie, Q.M. Su, G.H. Du, Ultrafine SnO₂ nanocrystals anchored graphene composites as anode material for lithium-ion batteries, *Mater. Res. Bull.* 68 (2015) 120–125.
- [17] X. Xu, S. Chen, C.H. Xiao, K. Xi, C.W. Guo, S.W. Guo, S.J. Ding, D.M. Yu, R. Vasant Kumar, Rational design of NiCoO₂@SnO₂ heterostructure attached on amorphous carbon nanotubes with improved lithium storage properties, *ACS Appl. Mater. Interfaces* 8 (2016) 6004–6010.
- [18] L. Zhang, H.B. Wu, S. Madhavi, H.H. Hng, X.W. Lou, Formation of Fe₂O₃ microboxes with hierarchical shell structures from metal-organic frameworks and their lithium storage properties, *J. Am. Chem. Soc.* 134 (2012) 17388–17391.
- [19] X. Qi, H.B. Zhang, J.T. Xu, X.Y. Wu, D.Z. Yang, J. Qu, Z.Z. Yu, Highly efficient high-pressure homogenization approach for scalable production of high-quality graphene sheets and sandwich-structured α -Fe₂O₃/graphene hybrids for high-performance lithium-ion batteries, *ACS Appl. Mater. Interfaces* 9 (2017) 11025–11034.
- [20] W.W. Zhou, C.W. Cheng, J.P. Liu, Y. Yan Tay, J. Jiang, X.T. Jia, J.X. Zhang, H. Gong, H.H. Hng, T. Yu, H.J. Fan, Epitaxial growth of branched α -Fe₂O₃/SnO₂ nano-heterostructures with improved lithium-ion battery performance, *Adv. Funct. Mater.* 21 (2011) 2439–2445.
- [21] X.S. Zhou, L. Yu, X.W. Lou, Formation of uniform N-doped carbon-coated SnO₂ submicroboxes with enhanced lithium storage properties, *Adv. Energy Mater.* 6 (2016) 1600451/1–6.
- [22] G.F. Xia, N. Li, D.Y. Li, R.Q. Liu, C. Wang, Q. Li, X.J. Lü, J.S. Spendelov, J.L. Zhang, G. Wu, Graphene/Fe₂O₃/SnO₂ ternary nanocomposites as a high-performance anode for lithium ion batteries, *ACS Appl. Mater. Interfaces* 5 (2013) 8607–8614.
- [23] P. Poizot, S. Laruelle, S. Grugnon, L. Dupont, J.M. Tarascon, Nano-sized transition-metal oxides as negative-electrode materials for lithium-ion batteries, *Nature* 407 (2000) 496–499.
- [24] A.S. Arico, P. Bruce, B. Scrosati, J.-M. Tarascon, W. Van Schalkwijk, Nanostructured materials for advanced energy conversion and storage devices, *Nat. Mater.* 4 (2005) 366–377.
- [25] H. Wu, G.H. Yu, L.J. Pan, N. Liu, M.T. McDowell, Z.N. Bao, Y. Cui, Novel rGO/ α -Fe₂O₃ composite hydrogel: synthesis, characterization and high performance of electromagnetic wave absorption, *Nat. Commun.* 4 (2013) 1943.
- [26] X. Zhu, Y. Zhu, S. Murali, M.D. Stoller, R.S. Ruoff, Nanostructured reduced graphene oxide/Fe₂O₃ composite as a high-performance anode material for lithium ion batteries, *ACS Nano* 5 (2011) 3333–3338.
- [27] D. Mhamane, V. Aravindan, D. Taneja, A. Suryawanshi, O. Game, M. Srinivasan, S. Ogale, Graphene based nanocomposites for alloy (SnO₂), and conversion (Fe₃O₄) type efficient anodes for Li-ion battery applications, *Compos. Sci. Technol.* 130 (2016) 88–95.
- [28] Y.H. Ding, B. Liu, R.S. Cai, T. Xin, C. Li, L.H. Xia, Y.Q. Wang, One-pot synthesis of α -Fe₂O₃ nanospindles as high-performance lithium-ion battery anodes, *Nano* 13 (2018) 1850018.
- [29] K.Z. Cao, L.F. Jiao, H.Q. Liu, Y.C. Liu, Y.J. Wang, Z.P. Guo, H.T. Yuan, 3D hierarchical porous α -Fe₂O₃ nanosheets for high-performance lithium-ion batteries, *Adv. Energy Mater.* 5 (2015) 1401421.
- [30] T. Yamashita, P. Hayes, Analysis of XPS spectra of Fe²⁺ and Fe³⁺ ions in oxide materials, *Appl. Surf. Sci.* 254 (2008) 2441–2449.
- [31] M.C. Ortega-Liebana, N.X. Chung, R. Limpens, L. Gomez, J.L. Hueso, J. Santamaria, T. Gregorkiewicz, Uniform luminescent carbon nanodots prepared by rapid pyrolysis of organic precursors confined within nanoporous templating structures, *Carbon* 117 (2017) 437–446.
- [32] D.A. Zatsepin, A.F. Zatsepin, D.W. Boukhalov, E.Z. Kurmaev, N.V. Gavrilov, Sn-loss effect in a Sn-implanted a-SiO₂ host-matrix after thermal annealing: a combined XPS, PL, and DFT study, *Appl. Surf. Sci.* 367 (2016) 320–326.
- [33] M. Madian, M. Klose, T. Jaumann, A. Gebert, S. Oswald, N. Ismail, A. Eychmüller, J. Eckert, L. Giebeler, Anodically fabricated TiO₂-SnO₂ nanotubes and their application in lithium ion batteries, *J. Mater. Chem. A* 4 (2016) 5542–5552.
- [34] H. Zhang, A.J. Xie, C.P. Wang, H.S. Wang, Y.H. Shen, X.Y. Tian, Novel rGO/ α -Fe₂O₃ composite hydrogel: synthesis, characterization and high performance of electromagnetic wave absorption, *J. Mater. Chem. A* 1 (2013) 8547–8552.
- [35] Z.X. Deng, C. Wang, X.M. Sun, Y.D. Li, Structure-directing coordination template effect of ethylenediamine in formations of ZnS and ZnSe nanocrystallites via solvothermal route, *Inorg. Chem.* 41 (2002) 869–873.
- [36] Y.D. Li, H.W. Liao, Y. Ding, Y.T. Qian, L. Yang, G.E. Zhou, Nonaqueous synthesis of CdS nanorod semiconductor, *Chem. Mater.* 10 (1998) 2301–2303.
- [37] S.Y. Zhang, P.G. Zhang, A.J. Xie, S.K. Li, F.Z. Huang, Y.H. Shen, A novel 2D porous print fabric-like α -Fe₂O₃ sheet with high performance as the anode material for lithium-ion battery, *Electrochim. Acta* 212 (2016) 912–920.
- [38] J.-M. Jeong, B.G. Choi, S.C. Lee, K.G. Lee, S.-J. Chang, Y.K. Han, Y.B. Lee, H.U. Lee, S. Kwon, G. Lee, C.-S. Lee, Y.S. Huh, Hierarchical hollow spheres of Fe₂O₃@polyaniline for lithium ion battery anodes, *Adv. Mater.* 25 (2013) 6250–6255.
- [39] D.M. Cui, Z. Zheng, X. Peng, T. Li, T.T. Sun, L.J. Yuan, Fluorine-doped SnO₂ nanoparticles anchored on reduced graphene oxide as a high-performance lithium ion battery anode, *J. Power Sources* 362 (2017) 20–26.
- [40] X. Zhou, L.-J. Wan, Y.-G. Guo, Binding SnO₂ nanocrystals in nitrogen-doped graphene sheets as anode materials for lithium-ion batteries, *Adv. Mater.* 25 (2013) 2152–2157.
- [41] Z.F. Wang, P.Y. Fei, H.Q. Xiong, C.L. Qin, W.M. Zhao, X.Z. Liu, CoFe₂O₄ nanoplates synthesized by dealloying method as high performance Li-ion battery anodes, *Electrochim. Acta* 252 (2017) 295–305.
- [42] G.M. Zhou, D.W. Wang, F. Li, L.L. Zhang, N. Li, Z.S. Wu, L. Wen, G.Q.M. Lu, H.M. Cheng, Graphene-wrapped Fe₃O₄ anode material with improved reversible capacity and cyclic stability for lithium ion batteries, *Chem. Mater.* 22 (2010) 5306–5313.
- [43] S. Chaudhari, M. Srinivasan, 1D hollow α -Fe₂O₃ electrospun nanofibers as high performance anode material for lithium ion batteries, *J. Mater. Chem.* 22 (2012) 23049–23056.
- [44] I.J. Gordon, S. Genies, G.S. Larbi, A. Boulineau, L. Daniel, M. Alias, Original implementation of electrochemical impedance spectroscopy (EIS) in symmetric cells: evaluation of post-mortem protocols applied to characterize electrode materials for Li-ion batteries, *J. Power Sources* 307 (2016) 788–795.
- [45] Y. Wang, Z.S. Feng, C. Zhang, L. Yu, J.J. Chen, J. Hu, X.Z. Liu, Defect effects on the physical and electrochemical properties of nanoscale LiFe_{0.92}PO₄ and LiFe_{0.92}PO₄/C/graphene composites, *Nanoscale* 5 (2013) 3704–3712.